Obstacle Detection of Intelligent Vehicle Based on Fusion of Lidar and Machine Vision

Binbin Sun, Wentao Li, Huibin Liu, Jinghao Yan, Song Gao and Penghang Feng

Abstract—**Obstacle detection is the key technology of environment perception for intelligent vehicle. To guarantee safe operation of an unmanned vehicle the fusion method of spatial information from lidar and machine vision is studied. The projection of the bounding box generated by lidar on machine vision image is designed. The detection area of obstacle is constructed. Moreover, the method of strong-classifier cascade connection is used to build a classifier. Specially, the Haar-like and HOG features within a huge amount of data are characterized based on AdaBoost algorithm. To achieve classification and recognition of the obstacles, the obstacle detection areas generated on the image are fused with the designed cascade classifier, and the effectiveness of the proposed fusion method is validated. Test results show that the obstacle detection method based on fusion of laser radar and machine vision shows higher detection accuracy. Under good weather conditions, compared with the detection method based on laser radar alone and based on machine vision alone, the proposed method increases the detection rate of vehicle obstacle by 18.33% and 12.74%, and increase the detection rate of pedestrian by 17.92% and 12.56%, respectively. Under the rainy weather, the detection rate of vehicle obstacle is improved by 38.44% and 14.28%, and the detection rate of pedestrian is enhanced by 29.34% and 15.84%, respectively.**

Index Terms—**unmanned vehicle, obstacle detection, data fusion, laser radar, machine vision**

I. Introduction

Autonomous drive technology of intelligent vehicle involves environment perception, path planning, intelligent decision and motion control [1-3]. Among them, environment perception is to obtain surrounding environment information of the vehicle through the on-board sensors, and then identify obstacles based on fusion of multi-source data, As a pre-condition for path planning, intelligent decision and motion control the environment perception is essential for the development of intelligent vehicle [4].

At present, three common modes are utilized to achieve environment perception for obstacle detection, including machine vision, millimeter-wave radar and data fusion of multiple sensors [5]. Data collected by camera affects machine vision-based obstacle detection results. The obstacle detection method based on machine vision has advantages of large detection range and perfect target information. However, it cannot obtain depth information [6]. Millimeter-wave radar has advantages of high resolution, high robustness to weather influence, and real-time feedback on relative position, speed and distance. However, the noise of such technology is too large to generate obstacle contour [7]. Under good weather conditions, lidar-based detection method of obstacle obtains a large amount of three-dimensional information of the environment directly, with small data noise and high measurement accuracy. However, the detection performance of such method is significantly decreased under bad weather [8].

Generally, a single sensor is inadequate to obtain sufficient driving environment information. Therefore, obstacle detection based on fusion of the information collected from dual or multi-sensors is designed. This advanced technology makes full use of multiple sensors, so it has improved perception accuracy and reliability [9]. Currently, data fusion between different kind of sensors has been commonly applied in practice, such as data fusion between millimeter wave radar and machine vision, data fusion between laser radar and machine vision, and so on [10].

As for obstacle detection based on fusion of millimeter wave radar and machine vision, the information about distance and angle of obstacle is confirmed by millimeter wave radar, and the obstacle recognition is realized via machine vision. However, such obstacle detection method shows high false warning rate and large missing rate target detection [11]. The obstacle detection method based on dual or triple machine visions uses the stereo camera to obtain the scale and contour data simultaneously, identifies the obstacle by V view, but fails to obtain depth information for path planning and intelligent decision making [12-13]. In contrast, using the obstacle detection method based on fusion of lidar and machine vision, the location of obstacle can be obtained by radar, and then the obstacle can be identified by image vision processing and classifier [14-15], so more accurate and comprehensive information can be obtained. However, the perception accuracy and real-time performance of the proposed method remain to be further improved due to the

Manuscript received October 26, 2020; revised March 26, 2021. This work was supported in part by the National Natural Science Foundation of China under Grant 51805301, the Natural Science Foundation of Shandong under Grant ZR2019BEE043, the Postdoctoral Science Foundation of China and Shandong under Grant 2020M680091 and 202003042, the key R & D projects in Shandong under Grant 2019GHZ016.

Binbin Sun, is professor of School of Transportation and Vehicle Engineering, Shandong University of Technology, Zibo, China (e-mail: sunbin_sdut@126.com).

Wentao Li, the corresponding author, is graduate student of School of Transportation and Vehicle Engineering, Shandong University of Technology, Zibo, China (e-mail: liwentao1213@126.com).

Huibin Liu, is graduate student of School of Transportation and Vehicle Engineering, Shandong University of Technology, Zibo, China (e-mail: 18764623813@163.com).

Jinghao Yan, is graduate student of School of Transportation and Vehicle Engineering, Shandong University of Technology, Zibo, China (e-mail: yanjinghao1111@163.com).

Song Gao, is professor of School of Transportation and Vehicle Engineering, Shandong University of Technology, Zibo, China (e-mail: gaos546@126.com).

Penghang Feng, is graduate student of School of Transportation and Vehicle Engineering, Shandong University of Technology, Zibo, China (e-mail: fengpenghang@saicmotor.com).

low processing speed of input data [15-16].

To this end, a dual-sensors fusion method based on a 3-D 32-line lidar and a monocular camera is proposed in this paper. By creating the area of interest for obstacle detection, it is possible to realize the extraction of Haar-like and HOG features, the design of cascade classifier, and obstacle detection in a real time manner. Specially, in chapter 1, the conversion of coordinate systems of laser radar and machine sensor is completed, and the projection method of bounding box generated by laser radar on machine vision image is proposed to construct obstacle detection area of interest. In Chapter 2, the method based on Haar-like and HOG features is designed to calculate the characteristic value of obstacle, and a cascaded classifier is created to detect obstacle. Chapter 3 presents details about test and data discussion.

II. Obstacle Detection Region of Interest

A. Fusion of Spatial Information from Laser Radar and Machine Vision

Four coordinate systems are designed in the machine vision system, including world coordinate system, camera coordinate system, imaging plane coordinate system and image pixel coordinate system. In this paper, the first one is defined as the body coordinate of the intelligent vehicle installed with camera. The camera coordinate system is created based on its center. The imaging plane and the pixel coordinate systems use physical and pixel units as benchmarks, respectively. There are two conversions of coordinate systems regarding the fusion of spatial information of lidar and machine vision. One is the three-dimensional transformation from world coordinate system to camera coordinate system. The other one is the conversion from camera coordinate system to pixel coordinate system. The transformation uses imaging plane coordinate system is used as an intermediate medium to realize the conversion form three-dimension to two-dimension.

Conversion from World Coordinate System to Camera Coordinate System

As shown in Figure 1, world and camera coordinates are illustrated. They are represented by $O\text{-}X_wY_wZ_w$ and $O\text{-}X_{cam}Y_{cam}Z_{cam}$, respectively. The transformation relationship between the two coordinates belongs to the Euclidean transformation, that is, one has rotation matrix R and the other one has translation vector T.

Therefore, for the same data in world coordinate and camera coordinate, the conversion is confirmed by the following formula.

$$\begin{bmatrix} x_{cam} \\ y_{cam} \\ z_{cam} \end{bmatrix} = R \begin{bmatrix} x_w \\ y_w \\ z_w \end{bmatrix} + T \tag{1}$$

The rotation matrix R is related to the installation position of camera, the heading angle φ, pitch angle δ, and roll angle ξ. T is determined by the camera installation position.

$$R = \begin{bmatrix} \cos\xi\cos\varphi & \sin\xi\cos\varphi & -\sin\varphi \\ -\sin\xi\cos\delta+\cos\xi\sin\varphi\cos\delta & \cos\xi\cos\delta+\sin\xi\sin\varphi\sin\delta & \cos\varphi\sin\delta \\ \sin\xi\sin\delta+\cos\xi\sin\varphi\cos\delta & -\cos\xi\cos\delta+\sin\xi\sin\varphi\cos\delta & \cos\varphi\cos\delta \end{bmatrix} \tag{2}$$

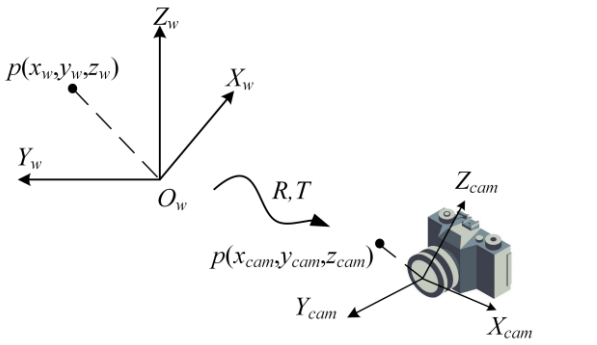

Fig. 1. The conversion from world coordinate system to camera coordinate system

Conversion from Camera Coordinate System to Pixel Coordinate System

Figure 2 shows the schematic of the camera aperture. Point O and o_1 represent the center of camera coordinate and the intersection of axis z and imaging plane, respectively. The distance between the two points is defined as f. The imaging and pixel coordinate systems are represented by $o_1\text{-}x_cy_c$ and $o_1\text{-}uv$, respectively. Furthermore, point Q is projected to q from three-dimensional space to imaging plane. According to the triangular proportional relationship, the relationship is expressed as:

$$x = f\frac{X}{Z} \tag{3}$$

$$y = f\frac{Y}{Z} \tag{4}$$

As shown in formula 5 and 6, the transformation relationship from point Q to point q can be expressed as $q=MQ$.

$$q = \begin{bmatrix} xZ \\ yZ \\ Z \end{bmatrix}, M = \begin{bmatrix} f & 0 & 0 \\ 0 & f & 0 \\ 0 & 0 & 1 \end{bmatrix}, Q = \begin{bmatrix} X \\ Y \\ Z \end{bmatrix} \tag{5}$$

Given the above analysis, the relationship between camera coordinate system and imaging plane coordinate system is expressed as:

$$Z\begin{bmatrix} x \\ y \\ z \end{bmatrix} = \begin{bmatrix} f & 0 & 0 \\ 0 & f & 0 \\ 0 & 0 & 1 \end{bmatrix}\begin{bmatrix} X \\ Y \\ Z \end{bmatrix} \tag{6}$$

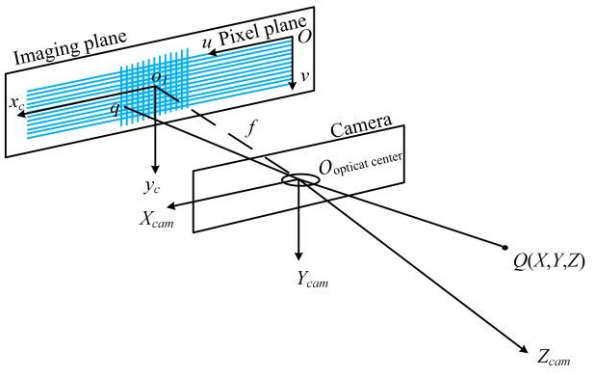

Fig. 2. Schematic of small-hole imaging model

In pixel plane, the size of each pixel is the product of *dx* and *dy*. Based on the following relationship, point *q* is converted from imaging plane coordinate system to pixel coordinate system.

$$u = \frac{x}{d_x} + u_0 \tag{7}$$

$$v = \frac{y}{d_y} + v_0 \tag{8}$$

Based on the above analysis, the data fusion of imaging plane coordinate system and pixel coordinate system is realized.

$$Z\begin{bmatrix} u \\ v \\ 1 \end{bmatrix} = K\begin{bmatrix} X \\ Y \\ Z \end{bmatrix} = \begin{bmatrix} \frac{f}{d_x} & 0 & u_0 \\ 0 & \frac{f}{d_y} & v_0 \\ 0 & 0 & 1 \end{bmatrix}\begin{bmatrix} X \\ Y \\ Z \end{bmatrix} \tag{9}$$

B. Detection Region of Interest Based on Data Fusion

Conversion from Lidar Coordinate System to World Coordinate System

In this paper, world coordinate system (O_w-$X_wY_wZ_w$) is used to characterize the coordinate of vehicle body. The centroid point of the vehicle is located on the origin of world coordinate system. Two coordinate systems are designed for lidar: one is the reference coordinate system (O_{lb}-$X_{lb}Y_{lb}Z_{lb}$) and the other one is the actual coordinate system (O_{lr}-$X_{lr}Y_{lr}Z_{lr}$). As shown in Figure 3, the two coordinate systems have different locations on axis Z. Therefore, the relationship of lidar and the vehicle body is confirmed by *R* and *T*.

$$\begin{bmatrix} P_x^{'} \\ P_y^{'} \\ P_z^{1} \end{bmatrix} = R\begin{bmatrix} P_x \\ P_y \\ P_z \end{bmatrix} + T + Z \tag{10}$$

where, *Z* and *T* are the translation vectors. Since the two origins discussed above are on the same axis z, *T* is defined as $[t_x, t_y, t_z]^T$.

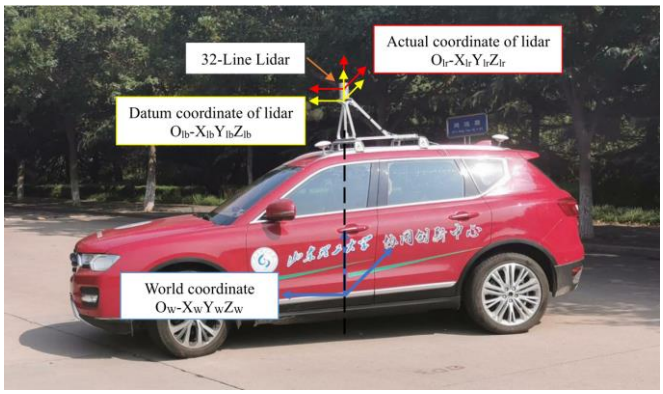

Fig. 3. The world coordinate, lidar reference coordinate and actual coordinate

During the installation process of lidar, the deviations of roll angle, pitch angle and deflection angle are unavoidable. The error of *R* will directly determine the error of the final return value of radar, so it is necessary to calibrate the radar accurately. In this study, the pitch angle is α, the roll angle is β', and the deflection angle is γ'. Since the radar is installed in the center of the longitudinal vertical plane of the vehicle body, only the calibration of α and β' is required:

As shown in Figure 4, a rectangular calibration plate is used to calibrate the roll angle of lidar.

The ∠FOE in Figure 4 is the azimuth difference between the edge points E and F of the radar and rectangular calibration plate. l_{OE}, l_{OF} represent the distance between point E and radar as well as that between the point F and radar, respectively. l_{EF} can be obtained according to the cosine theorem, then the roll angle β' can be expressed by Equation 11:

$$\beta^{'} = \arccos(\frac{l_{AB}}{l_{EF}}) \tag{11}$$

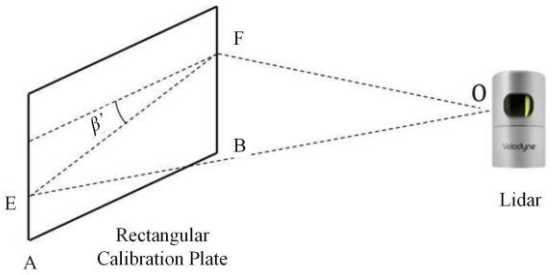

Fig. 4. The calibration of Lidar roll angle

The roll angle transformation matrix Ry of the radar is shown in Equation 12:

$$R_y = \begin{bmatrix} \cos\beta^{'} & 0 & \sin\beta^{'} \\ 0 & 1 & 0 \\ \sin\beta^{'} & 0 & \cos\beta^{'} \end{bmatrix} \tag{12}$$

The pitch angle is calibrated by using an isosceles triangle calibration plate. As shown in Figure 5. the triangular calibration plate is placed at A1, and ∠F_1OE_1, l_{OE1}, and l_{OF1} can all be acquired by radar data. Similarly, l_{EF1} can be obtained according to the cosine theorem.

$$l_{E_1Z_1} = l_{E_1F_1}\cos\gamma^{'} \tag{13}$$

$$l_{BZ_1} = l_{BC} - l_{E_1Z_1} \tag{14}$$

By moving the triangle calibration plate to A_2, l_{BZ2} can be obtained in the same way, and then the available radar elevation angle can be calculated as follow:

$$\alpha = \arctan(\frac{l_{BZ_1} - l_{BZ_2}}{l_{A_1A_2}}) \tag{15}$$

The transformation matrix R_x is:

$$R_x = \begin{bmatrix} 1 & 0 & 0 \\ 0 & \cos\alpha & \sin\alpha \\ 0 & -\sin\alpha & \cos\alpha \end{bmatrix} \tag{16}$$

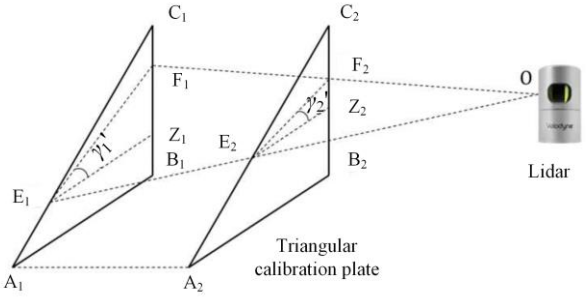

Fig. 5. The calibration of Lidar pitch angle

The points (P'_x, P'_y, P'_z) in the world coordinate system can be represented by the points (P_x, P_y, P_z) in the lidar coordinate system:

$$\begin{bmatrix} P_x' \\ P_y' \\ P_z' \end{bmatrix} = R_x R_y \begin{bmatrix} P_x \\ P_y \\ P_z \end{bmatrix} + T = \begin{bmatrix} 1 & 0 & 0 \\ 0 & \cos\alpha & \sin\alpha \\ 0 & -\sin\alpha & \cos\alpha \end{bmatrix} \begin{bmatrix} \cos\beta' & 0 & \sin\beta' \\ 0 & 1 & 0 \\ \sin\beta' & 0 & \cos\beta' \end{bmatrix} \begin{bmatrix} P_x \\ P_y \\ P_z \end{bmatrix} + T + Z \tag{17}$$

Bounding Box Projection on Machine Vision Images

As shown in Figure 6, the laser point cloud without ground is clustered by using the improved DBSCAN algorithm. By applying the obstacle bounding box to the machine vision projection, an obstacle can be generated to identify the detection region of interest. According to the conversion relationship between camera coordinate system and lidar coordinate system, the coordinate relation is defined as:

$$\begin{cases} u = -\dfrac{f}{d_x} \dfrac{Y_l}{(X_l - l_{wl})\sin\theta_c - (Z_l + h_l - h_c)\cos\theta_c} + u_0 \\ v = -\dfrac{f}{d_y} \dfrac{(X_l - l_{wl})\cos\theta_c + (Z_l + h_l - h_c)\sin\theta_c}{(X_l - l_{wl})\sin\theta_c - (Z_l + h_l - h_c)\cos\theta_c} + v_0 \end{cases} \tag{18}$$

where d_x and d_y represent the physical dimensions of the pixel points; l_{wl} is the distance between the origins of radar coordinate system and that of world coordinate system; h_l and h_c are the installation heights of the radar and camera, respectively; θ_c is the angle formed by the camera axis and vehicle cross section.

Based on the coordinate transformation relationship shown in the formula and the figure 6, the bounding box boundary points in the vertical plane formed by the lidar clustering can be projected into the image pixel plane to generate an obstacle recognition region of interest.

III. Obstacle Detection and Recognition in The Region of Interest Based on Machine Learning

A. Obstacle Feature Extraction and Calculation

Extraction and calculation of Haar-like features

Haar-like features include two rectangular features and three rectangular features. The black and white rectangular frames are defined as feature template. The three-matrixe feature template is composed of one black and two white rectangular frames. In this paper, the feature value size is confirmed by the difference value between the black and white rectangular areas. The dynamic window length and width in the region of interest are represented by L and W, respectively. The Haar-like feature value is calculated by Equation 19.

$$Haar = \sum_{k=1}^{N} \omega_k Sum(r_k), (0 \le x, x+l \le L, 0 \le y+w \le W) \tag{19}$$

where N is the number of feature rectangles, ω_k is the weight value, $Sum(r_k)$ is the sum of all pixel values in the rectangle, r represents any matrix region within the window.

In practical engineering the entire region of interest needs to be traversed, and the real-time performance of the algorithm is influenced by the calculation of the pixel value. Consequently, the principle of integral graph is used to ensure the real-time performance, as shown in Equation 20.

$$II(x, y) = \sum_{i \le x, j \le y} f(i, j) \tag{20}$$

where $f(i, j)$ represents the image pixel value.

The recursive calculations are applied to increase the speed of the algorithm.

$$\begin{cases} II(x, y) = II(x, y-1) + II(x-1, y) - II(x-1, y-1) + f(x, y) \\ II(x, x-1) = II(-1, y) = II(-1, -1) = 0 \end{cases} \tag{21}$$

The calculation process is traversed using the first row and the last column. First, calculate the integral map, that is, calculate all the pixels in the upper left area of the current position, and then use the integral map to accelerate the calculation of the pixel sum in a matrix. As shown in Figure 7, the sum of the pixels of the D area can be represented by *Sum*(1)+*Sum*(4)-*Sum*(2)-*Sum*(3).

Extraction and Calculation of HOG Features

The extraction and calculation algorithm of Haar-like feature designed above has real-time performance. However, the method is unable to reflect the complex features of the object effectively. To balance between detection speed and detection accuracy, the extraction and calculation of *HOG* features are fused. Based on cell unit, the image is divided by *HOG* features. Then, the gradient direction histogram of each cell unit is calculated and the cell unit is normalized to obtain the *HOG* features. The gradient direction distribution of local image reflects significant features (such as shape) of the target in the image, which is the core of the algorithm. The process for extracting and calculating *HOG* features is as follows.

Step1: Grayscale processing of the input image;

Step2: Based on the Gramma correction method, the input image is normalized to reduce the influence of factors such as lighting conditions.

$$G(x, y) = F(x, y)^{\frac{1}{\gamma}} \tag{22}$$

When γ is taken as 0.5, the pixel range is converted from 0~255 to 0 ~ 15.97.

Step3: This step is designed to confirm the size and direction of pixel gradient. The gradient is derived as:

$$GM(x, y) = \sqrt{[f(x+1, y) - f(x-1, y)]^2 + [f(x+1, y) - f(x-1, y)]^2} \tag{23}$$

The gradient direction is confirmed as:

$$GD(x, y) = \begin{cases} GD^*(x, y) + \pi, GD^*(x, y) < 0 \\ GD^*(x, y), others \end{cases} \tag{24}$$

where $GD^*(x, y)$ is:

$$GD^*(x, y) = \arctan \frac{f(x, y+1) - f(x, y-1)}{f(x+1, y) - f(x-1, y)} \tag{25}$$

Step4: The image is divided into N rectangular blocks. First of all, the gradient direction is mapped within 180°. Then, the mapped region is divided from 0° to 180° based on the number of N_{GD} intervals. The gradient direction histogram is expressed by the following formula:

$$CV(Cell, k) = \sum_{(x, y) \in Block} V_k(x, y), k = 1, 2, \cdots, N_{GD} \tag{26}$$

where CV ($Cell$, k) represents the cumulative value of the gradient size of cell in the K direction interval; V_k (x, y) is the gradient size of (x, y) in the K direction interval.

Step5: Normalize the calculation of the cell:

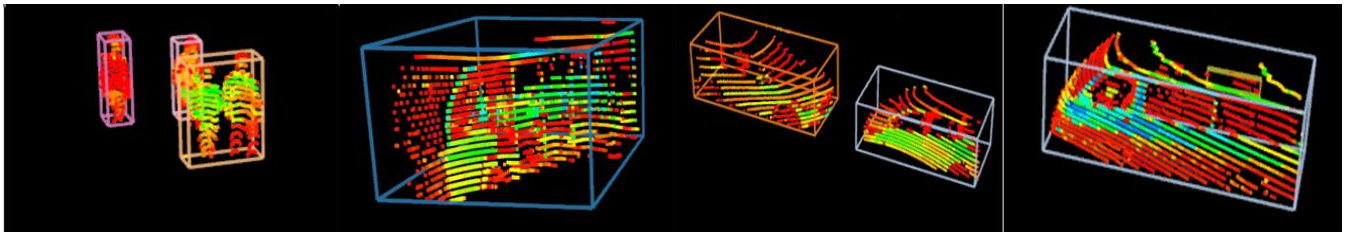

(a) (b) (c) (d)

Fig. 6. Improved DBSCAN clustering and generation of Bounding Box

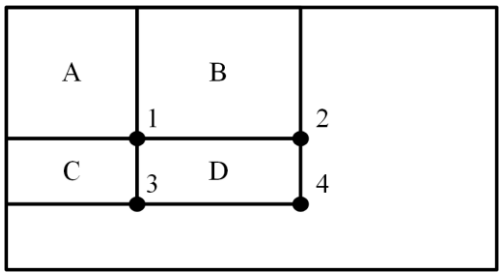

Fig. 7. Integral map definition map

$$HOGFea = [BD(Cell,1)\cdots BD(Cell,k)\cdots BD(Cell,N_{GD})]^T \tag{27}$$

where $BD(Cell, k)$ is:

$$BD(Cell,k) = \frac{CV(Cell,k)}{\sum_{k=1}^{N_{GD}} CV(Cell,k) + \varepsilon} \tag{28}$$

where ε is a minimum value that is set to prevent the denominator from being 0.

Step6: Statistical gradient histogram. The *HOG* feature is the result of concatenating the feature vectors of all blocks in the window. In order to improve the calculation speed, the *HOG* eigenvalue is calculated by using the gradient histogram in integral direction. The integral graph principle is shown in Equations 21 and 22.

B. Obstacle Recognition Based on AdaBoost Cascade Classifier

The AdaBoost algorithm involves both weak classifiers and strong classifiers. The weak classifier obtains arbitrary precision classifier through certain combinations, but target recognition rate is unsatisfactory. The strong classifier has a high recognition rate,but its the real-time performance is limited unsatisfactory due to the long classification time. As the lidar points are projected onto the region of interest, there are still obstacle categories that do not contain the current detection. Using a strong classifier may lead to an overlong classification time. Therefore, this paper uses a cascade classifier from weak classifier to strong classifier. The core idea is to process the sub-window of the region of interest based on the AdaBoost algorithm. Only when the classification obstacle is consistent with the target obstacle, it will be input to the next-level strong classifier. Otherwise, it is directly output as a non-target obstacle.

Strong Classifier Training Based on AdaBoost

The process is divided into the following steps:

Step1: Giving a training sample set. This paper stipulates that $S=\{(x_1,y_1)$, (x_2,y_2) ,..., (x_i,y_i) ,..., $(xN_s,yN_s)\}$ are sample sets, positive samples are y_i=1, total Np, negative samples. The rule is y_i=-1, a total of N_N. Where i=1, 2, .., Ns, N_F features are extracted for each sample.

Step2: Initialize the weight of the training sample.

$$G_1 = \{\omega_{11},\omega_{12},\cdots,\omega_{1i},\cdots,\omega_{1N_S}\} \tag{29}$$

$$\omega_{1i} = \begin{cases} \frac{1}{2N_P}, y_i = 1 \\ \frac{1}{2N_N}, y_i = -1 \end{cases} \tag{30}$$

Step3: For the t-th iteration:

1. According to the sample set S under the training sample weight distribution calculated in step 2, the weak classifier $h_j(x)$ is obtained;

2. The error rate of weak classifier is obtained by the following formula:

$$e_j = \sum_{i=1}^{N_S} \omega_{ti} I_A(h_j(x_i) - y_i), j = 1,2,\cdots,N_F \tag{31}$$

$$A = \{x \in R | x \neq 0\} \tag{32}$$

where I_A reflects the positive and negative of A.

3. Select the e_t with the smallest error rate, and corresponding weak classifier can be obtained, and then select the current threshold.

$$\alpha = \frac{1}{2}\ln\frac{1-e_t}{e_t} \tag{33}$$

4. Update the weight of the S sample set:

$$G_{t+1} = \{\omega_{t+1,1},\omega_{t+1,2},\cdots,\omega_{t+1,i},\cdots,\omega_{t+1,N_S}\} \tag{34}$$

$$\omega_{t+1,j} = \frac{\omega_{ti} e^{-\alpha_t y_i h_t(x_i)}}{\sum_{i=1}^{N_S} \omega_{ti} e^{-\alpha_t y_i h_t(x_i)}}, i = 1,2,\cdots,N_S \tag{35}$$

5. Finally, a strong classifier is obtained:

$$H(x) = sign(\sum_{t=1}^{T} \alpha_t h_t(x)) \tag{36}$$

Weak Classifier and Its Training Process

In order to minimize the sample error rate, it is necessary to obtain an optimal weak classifier of which the threshold θ and offset P_j are given. Then, multiple weak classifiers can be combined into one strong classifier. The weak classifier can be determined by the following formula:

$$h_j(x) = \begin{cases} 1, p_j f_j(x) < p_j \theta_j \\ -1, others \end{cases} \tag{37}$$

where $h_j(x)$ is the judgment value; x represents the sub-window of the input image; $f_j(x)$ is the j-th eigenvalue; θ means the threshold of weak classifier; P_j represents the direction of inequality. As the classification result is larger than θ, P_j is less than the positive value.

Four steps are designed to achieve the training of weak classifier.

Step1: Find all feature values *j* and arrange them in order of size;

Step2: Traverse the ordered feature values in Step1. Calculate the weights of all positive and negative samples as well as the weights of S^+ and S- and all positive and negative samples before the *i*-th sample and $S^+{}_i$ and $S^-{}_i$;

Step3: Select a certain number in the interval composed of the feature value $f_j(x_i)$ of the current sample *i* and the feature value $f_j(x_{i-1})$ of the previous sample *i*-1 as the threshold value θ_{lj}, and the deviation of the threshold value can be obtained as follow:

$$e_j^i = \min(e^-, e^+) \tag{38}$$

$$\begin{cases} e^- = S_i^+ + (S^- - S_i^-) \\ e^+ = S_i^- + (S^+ - S_i^+) \end{cases} \tag{39}$$

Step4：Repeat Step2 and Step3 to traverse the entire training sample set *S* so as to find the optimal threshold e^i_j with the smallest classification error.

Classifier Cascade

In this paper, both detection speed and detection what are taken into account. The cascade classifier allows each input image to pass through in sequence. For a given image, it has to pass the test of the strong classifier. Otherwise, it is unable to enter the subsequent strong classifier detection. In this way, the picture area of all detectors is the effective obstacle area. Detailed steps are as follows:

Step1: The positive and the negative sample sets are defined as V_P and V_N, respectively.

Step2: The number of cascaded classifier layers is represented by $K = log\, f_{max} F_{max}$.

Step3: If $k<K$, the training set is detected sequentially by the trained strong classifiers H_1, H_2, ... H_k. A sample with positive detection results is placed in V_{Pk+1} as a positive sample for the k+1th strong classifier training. A sample with a negative sample set. Which misdetected as a positive result, is placed in V_{Nk+1} as a negative sample for the *k*+1th strong classifier training.

Step4: If and only if the number of samples of V_{Pk+1} reaches N_p, the number of samples of V_{Nk+1} stops when it reaches N_N.

Step5: The final cascade classifier is determined until $k=K$.

IV. Test Verification

A. Camera Calibration Experiment

A calibration plate is made using MATLAB code, printed out and then attached to a square plate. Each square side measured by the test is 34 mm long. Then, the camera is activated in the system to capture calibration plate images at different angles and positions. As shown in Figure 8, 30 calibration plate images are collected in the test. The parameters of the camera used in the test are presented in table I.

TABLE I
Camera Parameters

INDEX	PARAMETE	UNIT
resolution	1920×1200	px
Pixel size	5.86×5.86	um
frame rate	40	fps
power	3	w
target size	1/1.2	in
case temperature	0-50	℃
weight	90	g
supply voltage	12-24	v

Figure 9 (a) shows the measured external position parameter map. Figure 9 (b) shows the average error histogram. The highest average error is 0.6. The average error of all pictures is 0.41, which is less than the average value 0.5. Therefore, the camera calibration meets the test requirements.

Based on the test results, the camera internal reference matrix is determined as:

$$K = \begin{bmatrix} 4137.8253 & 0 & 1028.3483 \\ 0 & 4147.3578 & 616.3249 \\ 0 & 0 & 1 \end{bmatrix} \tag{40}$$

The camera's rotation matrix and translation vector are:

$$R = \begin{bmatrix} 0.95 & -0.06 & 0.18 \\ 0.03 & -0.53 & -0.66 \\ 0.18 & 0.66 & -0.52 \end{bmatrix} \tag{41}$$

$$T = \begin{bmatrix} 227.6 \\ -216.5 \\ 535.7 \end{bmatrix} \tag{42}$$

B. Identification of Areas of Interest

For the pixel points on *x* axis and *y* axis, the physical dimensions are 5.86um and 4.37um. The distance between radar and world coordinate system is l_{wl}=1594.9mm. The installation height of the radar and camera are 2200mm and 1580mm, respectively. The camera is mounted with a pitch angle θ_c=76.158°, u_0=1028.3483, v_0=616.3296. In summary, transformation relations are confirmed.

$$\begin{cases} u = -4137.8253 \dfrac{Y_l}{0.9710 \times (X_l - 1597.9) - (Z_l + 620)} + 1028.3483 \\ v = -4147.3587 \dfrac{0.2392 \times (X_l - 1597.9) + 0.9710 \times (Z_l + 620)}{0.9710 \times (X_l - 1597.9) - 0.2392 \times (Z_l + 620)} + 616.3249 \end{cases} \tag{43}$$

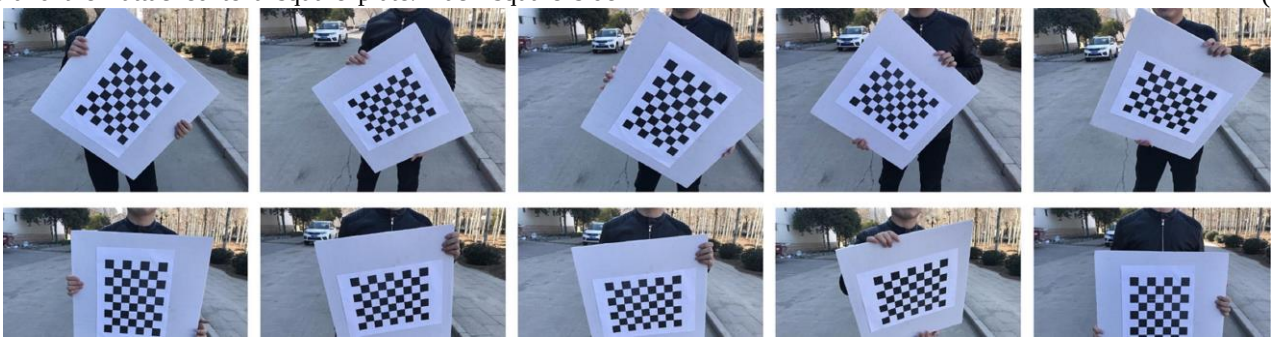

Fig. 8. Calibration plate image

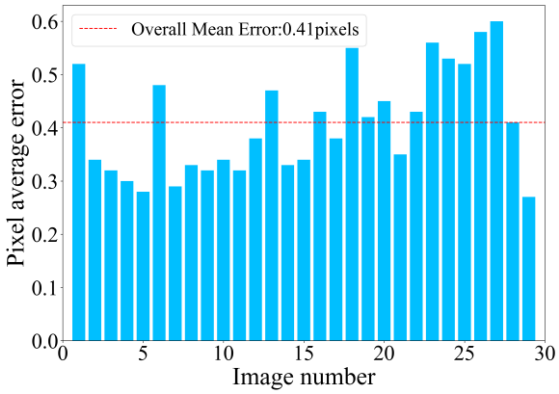

(a)Histogram of average projection error

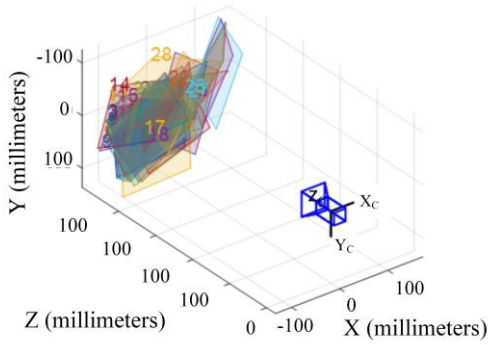

(b) External location parameter map

Fig. 9. Camera calibration results

By substituting the projection of the bounding box obtained by the laser radar into the boundary point (Y_l, Z_l) of the *YOZ* plane into the equation 42 corresponding four pixel points in the pixel plane of the image can be obtained so as to realize its projection on the image. The experimental radar technical parameters are shown in Table 2. The area formed by the four pixels is the area of interest. In the original image captured by the camera, the region of interest projected by the bounding box in the upper section is separately intercepted and imported into the classifier for detection and identification.

TABLE II
LINE LIDAR PARAMETERS

INDEX	PARAMETE	UNIT
accuracy	±2	cm
harness	32	line
vertical distance	80-100	m
vertical range	-30~10	degree
update frequency	10	Hz
weight	1	Kg
number of point clouds	700000	point / s
horizontal range	360	degree
power	12	w
vertical angular resolution	1.33	degree

C. Classification of Obstacles in Camera Raw Images using AdaBoost Classifier

An enormous number of training samples are prepared to ensure the reliability of vehicle information. When constructing the training set, the positive sample design occupies a larger proportion of the picture at the tail of the vehicle, the negative sample is designed to exclude all other images of the vehicle, and the negative sample occupies more sample proportion than the positive sample. In this paper, the intercepted image and the open-source data set of the experimentally collected video stream are combined as a training set, and the total number of positive sample images is 1582. Since the images collected contain the experiment have other targets in addition to the vehicle target, the positive sample images need to be intercepted, in order to make the vehicle information in each positive sample image fill the entire image as much as possible and reduce the influence of other invalid features in the training process.

The negative sample consists of 7786 pictures. To achieve perfect training results, the proportion rate of positive sample and negative sample is higher than 1:5 in the AdaBoost cascade classifier. Since there is no vehicle in the image, the negative sample includes buildings, guardrails, signage, flowers and trees, and other targets. Parts of the original images collected by the experimental vehicle on the campus are imported into the classifier for identification and detection. The detection effect is shown in Figure 10.

Tables 3 and 4 show the classification results for the three obstacle detection schemes under good weather conditions. Among them, scheme 1 is obstacle detection based on laser radar, scheme 2 is machine vision-based obstacle detection via direct input of the original image, and scheme 3 is the obstacle detection based on the dual sensor fusion and the AdaBoost classifier. Since the original image input by the camera does not reject targets outside the road boundary, the total number of vehicles and pedestrians using the camera alone is larger than that obtained by other two technical routes. For obstacle vehicle detection, scheme 1 has the shortest average detection time per frame. However, scheme 1 only reflects the general outline of the vehicle, and its detection rate is lower than that of scheme 2 and scheme 3 by 4.71% and 15.48%, respectively. Scheme 3 eliminates the invalid area of the image, so the detection rate is increased by 12.74%, and the average detection time per frame is reduced by 25.60% compared with the scheme 2.

TABLE III
OBSTACLE VEHICLE DETECTION RESULTS UNDER DIFFERENT TECHNICAL ROUTES

scheme	sensor type	total number of targets	checkout number	detecti on rate	average detection time per frame
1	laser radar	986	792	80.32%	22.65ms
2	camera	891	751	84.29%	47.23ms
3	camera and laser fusion	1006	956	95.03%	35.14ms

TABLE IV
DETECTION RESULTS OF PEDESTRIANS UNDER DIFFERENT TECHNICAL ROUTES

scheme	sensor type	total number of targets	checkout number	detecti on rate	average time per frame
1	laser radar	1346	1056	78.45%	22.69ms
2	camera	1594	1309	82.12%	54.36ms
3	camera and laser fusion	1468	1358	92.51%	43.12ms

For the detection of pedestrians, scheme 1 has the shortest average detection time per frame. However, scheme 1 only reflects the general outline of pedestrians, its detection rate is lower than that of scheme 2 and scheme 3 by 4.47% and 15.20% respectively. Since scheme 3 eliminates the invalid area of the image, its detection rate is 12.56% higher and average detection time per frame is 20.68% lower compared with scheme 2.

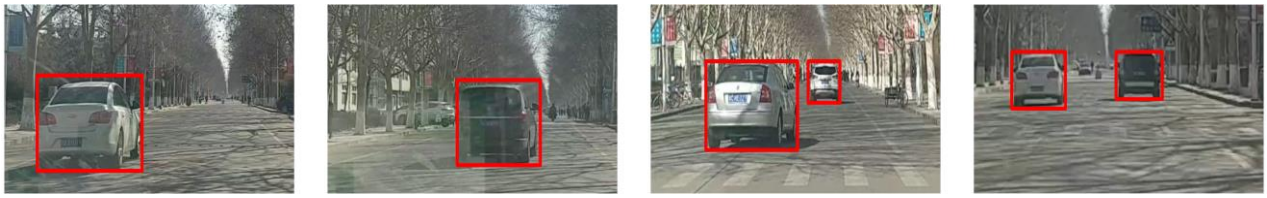

(a) Vehicle classification results

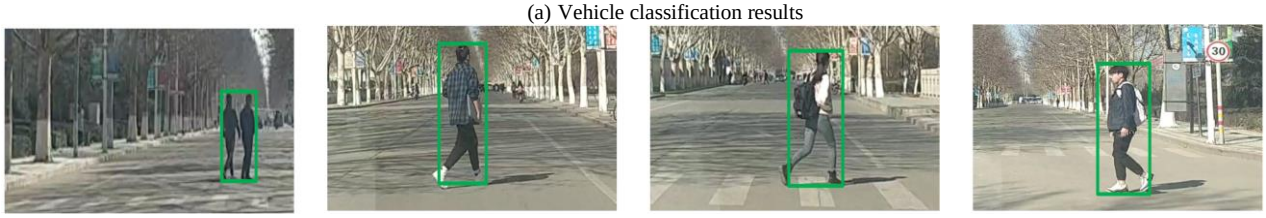

(b) Pedestrian classification results

Fig. 10. Classification result of classifier

Tables 5 and 6 show the classification results of the three obstacle detection methods under rainy weather conditions. Due to the influence of rainy weather, the detection rate of obstacle vehicles of the three detection schemes is lower than that under good weather conditions by 18.69%, 6.13% and 4.85%, respectively. Scheme 1 is most significantly affected by weather conditions. Scheme 1 has the shortest average detection time per frame, However, it only reflects the general outline of the vehicle, so its detection rate is lower than that of scheme 2 and scheme 3 by 17.45% and 27.78% respectively. Since scheme 3 eliminates the invalid area of the image, so the detection rate is improved by 14.28% and the average detection time per frame is reduced by 22.4% compared with scheme 2.

TABLE V
VEHICLE DETECTION RESULTS OF LASER RADAR, CAMERA, CAMERA AND LASER FUSION

scheme	sensor type	total number of targets	checkout number	detecti on rate	Average detection time per frame
1	laser radar	695	741	65.31%	22.32ms
2	camera	646	778	79.12%	47.72ms
3	camera and laser fusion	612	804	90.42%	37.03ms

TABLE VI
DETECTION PEDESTRIAN RESULTS OF LASER RADAR, CAMERA, CAMERA AND LASER FUSION

scheme	sensor type	total number of targets	checkout number	detecti on rate	average time per frame
1	laser radar	312	980	70.71%	20.04ms
2	camera	375	1240	80.31%	49.12ms
3	camera and laser fusion	346	1056	91.46%	41.34ms

For the pedestrian detection, the detection rate of the three schemes under rainy weather is lower than that under good weather conditions by 9.87%, 2.21% and 1.13%, respectively. Scheme 1 is most significantly affected by weather conditions, followed by scheme 2. The detection rate of vehicle obstacle is higher than the detection rate of pedestrian obstacle for all three schemes, which is mainly due to that the total number of pedestrian obstacles in the rainy weather is less than that of vehicle obstacles. Scheme 1 has the shortest average detection time per frame. However, it only reflects the general outline of pedestrians, so the detection rate is lower than that of scheme 2 and scheme 3 by 11.95% and 22.69% respectively. Scheme 3 eliminates the invalid area of the image, so the detection rate is higher by 13.88% and the average detection time per frame is decreased by 15.84% compared with scheme 2.

V. CONCLUSION

This paper studies the sensor-fusion obstacle detection method based on 3D 32-line laser radar and monocular camera. The following conclusions are drawn from this study:

(1) Unlike traditional approach, the region of interest is detected by laser radar and machine vision to generate obstacles, which are then input into AdaBoost classifier for classification. The proposed method is able to achieve a balance between detection accuracy and detection speed. Under good weather, the detection rate of vehicle obstacle and pedestrian obstacle increases by 12.74% and 12.56%, the average detection time per frame decreases by 25.60% and 20.68%, respectively. Under rainy weather, the detection rate of vehicle obstacle and pedestrian obstacle increases by 14.28% and 13.88%, the average detection time per frame decreases by 22.4% and 15.84%, respectively.

(2) Compared with obstacle detection based on lidar, the obstacle detection based on fusion of lidar and machine vision has significantly increased obstacle detection rate. Under good weather conditions, the detection rate of vehicle obstacle and pedestrian obstacle increases by 18.33% and 17.92%, respectively. Under rainy weather conditions, the value increases by 38.44% and 29.34%, respectively.

(3) Under rainy weather conditions, the obstacle detection based on fusion of lidar and machine vision has a high false detection rate. Therefore, further research on the fusion of laser radar, machine vision (binocular) and millimeter wave radar is needed.

REFERENCES

[1] JessicaVan Brummelen, MarieO'Brien, Dominique Gruyer, Homayoun Najjaran, "Autonomous Vehicle Perception: The Technology of Today and Tomorrow," Transportation Research Part C: Emerging Technologies, vol. 89, pp384-406, 2018.

[2] Weijing Shi, Mohamed Baker Alawieh, Xin Li, Huafeng Yu, "Algorithm and Hardware Implementation for Visual Perception System in Autonomous Vehicle: A Survey," Integration, vol. 59, pp148-156, 2017.

[3] Dominique Gruyer, Valentin Magnier, Karima Hamdi, Laurène Claussmann, Olivier Orfila, Andry Rakotonirainy, "Perception, Information Processing and Modeling: Critical Stages for Autonomous Driving Applications," Annual Reviews in Control, vol. 44, pp323-341, 2017.

[4] D. Hermann, R. Galeazzi, J. C. Andersen, M. Blanke, "Smart Sensor Based Obstacle Detection for High-Speed Unmanned Surface Vehicle," IFAC-PapersOnLine, vol. 48, no.16, pp190-197, 2015.

[5] Jacopo Guanetti, Yeojun Kim, Francesco Borrelli, “Control of Connected and Automated Vehicles: State of the Art and Future Challenges,” Annual Reviews in Control, vol. 45, pp18-40, 2018.
[6] P. V. Manivannan, Pulidindi Ramakanth, “Vision Based Intelligent Vehicle Steering Control Using Single Camera for Automated Highway System,” Procedia Computer Science, vol. 133, pp839-846, 2018.
[7] PEI Xiaofei, LIU Zhaodu, MA Guocheng, YE Yang, “Safe Distance Model and Obstacle Detection Algorithms for A Collision Warning and Collision Avoidance System,” Journal of Automotive Safety and Energy, vol. 3, no.1, pp26-33, 2016.
[8] Liang Wang, Yihuan Zhang, Jun Wang, “Map-Based Localization Method for Autonomous Vehicles Using 3D-LIDAR,” IFAC-PapersOnLine, vol. 50, no.1, pp276-281, 2017.
[9] Chen, S., Huang, L., Bai, J., Jiang, H. et al., "Multi-Sensor Information Fusion Algorithm with Central Level Architecture for Intelligent Vehicle Environmental Perception System," SAE Technical Paper 2016-01-1894, 2016.
[10] Guan Xin, Hong Feng, Jia Xin, Zhang Yonghe, Bao Han, “A Research on the Environmental Perception Method in Intelligent Vehicle Simulation Based on Layered Information Database,” Automotive Engineering, vol. 37, no.1, pp43-48, 2015.
[11] Wang T, Zheng N, Xin J, et al., “Integrating Millimeter Wave Radar with a Monocular Vision Sensor for On-road Obstacle Detection Applications,” Sensors, vol. 11, no.9, pp8992-9008, 2011.
[12] M. Bertozzi, A. Broggi, A. Fascioli and S. Nichele, “Stereo vision-based vehicle detection,” Proceedings of the IEEE Intelligent Vehicles Symposium 2000 (Cat. No.00TH8511), pp39-44, 2000.
[13] Zhang Yi, “Stereo-based Research on Obstacles Detection in Unstructured Environment,” Master's thesis, Beijing Institute of Technology, Beijing, China, 2015.
[14] Mahlisch M, Schweiger R, Ritter W, et al., “Sensorfusion Using Spatio-Temporal Aligned Video and Lidar for Improved Vehicle Detection,” 2006 IEEE Intelligent Vehicles Symposium, pp424-429, 2006.
[15] Zhang Shuangxi, “Research on Obstacle Detection Technology Based on Radar and Camera of Driverless Smart Vehicles,” Master's thesis, Chang’an University, Xi’an, China, 2013.
[16] Wang Z, Chen B, Wu J, et al., “Real-time Image Tracking with An Adaptive Complementary Filter,” IAENG International Journal of Computer Science, vol. 45, no.1, pp97-103, 2018.